Scaling of Kondo spin relaxation: Experiments on Cu-based nonlocal spin valves with Fe impurities

Xingyu Shen and Yi Ji*

Department of Physics and Astronomy, University of Delaware, Newark, Delaware 19716, USA

(Received 23 December 2020; revised 21 June 2021; accepted 13 July 2021; published 2 August 2021)

The relation between the Kondo spin-relaxation rate ${\tau_{sK}}^{-1}$ and the Kondo momentum-relaxation rate ${\tau_{eK}}^{-1}$ is explored by using nonlocal spin valves with submicron copper channels that contain dilute iron impurities. A linear relation between ${\tau_{sK}}^{-1}$ and ${\tau_{eK}}^{-1}$ is established under varying temperatures for any given device. Among 20 devices, however, ${\tau_{sK}}^{-1}$ remains nearly constant, despite variation of ${\tau_{eK}}^{-1}$ by a factor of 10. This surprising relation can be understood by considering spin relaxation through overlapping Kondo screening clouds and supports the physical existence of the elusive Kondo clouds.

DOI: 10.1103/PhysRevB.104.085101

I. INTRODUCTION

The Kondo effect [1,2] has captured attention for decades because of its complex many-body physics. In metals with dilute magnetic impurities, the signature of Kondo effect is the low-temperature increase of resistivity resulting from the antiferromagnetic *s-d* exchange interaction between the impurity spin and the conduction electron spins of the host metal. A popular but controversial physical picture is the Kondo screening cloud, which is an electron cloud surrounding the impurity site with an overall spin polarization opposite to the impurity spin. At temperatures well below the Kondo temperature T_K, the net spin of the Kondo cloud completely screens the impurity spin, forming a Kondo singlet state. Its spatial extent ξ_K is given theoretically by $\hbar v_F/k_BT_K$ in the ballistic transport regime and $\sqrt{\hbar D/k_BT_K}$ in the diffusive regime [3,4], where v_F is the Fermi velocity, k_B the Boltzmann constant, and D the diffusion constant.

Consider Fe impurities in Cu host ($T_K = 30$ K) as an example. The ξ_K is 400 nm in the ballistic regime and $\sim$100 nm in the diffusive regime. The average distance between Fe impurities at 1 part per million (ppm) in Cu is $\sim$20 nm and significantly smaller than ξ_K. This leads to a somewhat unsettling implication that Kondo clouds from neighboring impurities overlap substantially even at a very low concentration [5]. The size and configuration of Kondo clouds are challenging to probe experimentally, because the spin density is extremely dilute: $\sim$ 1 Bohr magneton per $(100\,\mathrm{nm})^3$ volume. The physical existence of Kondo clouds has been questioned [3,6,7]. Recently, Borzenets *et al*. [8] found convincing evidence for micrometer-sized Kondo clouds in a semiconductor quantum dot [9] system. However, evidence for Kondo clouds in metals is still lacking.

In recent years, the Kondo effect crosses paths with spintronics. In the Cu channels of nonlocal spin valves (NSLVs) [10,11] with dilute Fe impurities, the spin-relaxation rate ${\tau_s}^{-1}$ is found to increase at low temperatures, complementing the Kondo effect's low-temperature increase of the momentum-relaxation rate ${\tau_e}^{-1}$ [12–15]. Here τ_s and τ_e are the spin-relaxation time and momentum-relaxation time, respectively. For spin relaxation in general, Elliott-Yafet (EY) [16,17] and Dyakonov-Perel (DP) [18] models give explicit relations between ${\tau_s}^{-1}$ and ${\tau_e}^{-1}$. The EY spin relaxation is caused by weak spin-orbit coupling between energy bands, and ${\tau_s}^{-1}$ is proportional to ${\tau_e}^{-1}$. The ratio τ_e/τ_s is the spin-flip probability α. The DP spin relaxation originates from spin-orbit coupling, caused by inversion symmetry breaking, between two spin subbands within the same energy band, and the ${\tau_s}^{-1}$ is inversely proportional to ${\tau_e}^{-1}$. The Kondo spin relaxation, however, is caused by *s-d* exchange interaction instead of spin-orbit effects.

In this work we use a systematic method to extract the Kondo spin-relaxation rate ${\tau_{sK}}^{-1}$ and Kondo momentum-relaxation rate ${\tau_{eK}}^{-1}$ from each NLSV device. A relation between ${\tau_{sK}}^{-1}$ and ${\tau_{eK}}^{-1}$ is established by using a set of 20 NLSVs. The ${\tau_{sK}}^{-1}$ is independent of ${\tau_{eK}}^{-1}$, as the latter varies over a substantial range. We provide a qualitative explanation of this unusual relation by considering the spin density and charge density of overlapping Kondo clouds as well as the spin and momentum-relaxation processes through the clouds.

II. SAMPLE PREPARATION AND MEASUREMENTS

Our NLSVs are fabricated by two-step electron-beam lithography. Each NLSV includes a spin injector F_1, a spin detector F_2, and a Cu channel, as shown in Fig. 1(a). Magnetic electrodes F_1 and F_2, made of $Ni_{81}Fe_{19}$ alloy (permalloy or Py), are patterned in the first step, and Cu channels are patterned in the second step. The materials are deposited by electron-beam evaporation. The widths of F_1 and F_2 are 160 and 120 nm, respectively, and the thickness is 35 nm. Before the deposition of Cu, low-energy ion milling is performed to clean the surface of Py and a 3-nm AlO_x layer is deposited. The Py/AlO_x/Cu interfaces have been shown to provide a higher effective spin polarization than the Ohmic Py/Cu interfaces [19,20]. The distance L between F_1 and F_2 varies from 1 to 5 μm with 1-μm increments. All Cu channels are

*yji@udel.edu

 ©2021 American Physical Society

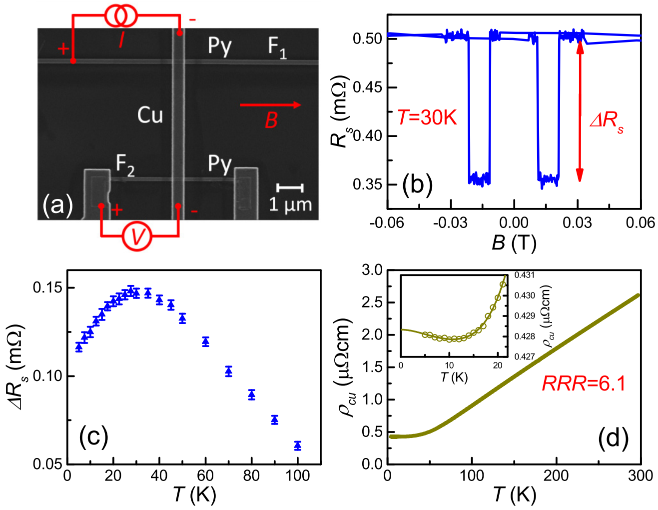

FIG. 1. (a) Scanning electron microscopy image of a NLSV. Plots of (b) R_s vs B, (c) ΔR_s vs T, and (d) $\rho_{\rm Cu}$ vs T for device 11-43 ($L = 3.0\,\mu$m).

500 nm wide and 300 nm thick to prevent the suppression of Kondo clouds [7,21]. This work involves data from two sample substrates (chips 11 and 12) with ten devices on each. Devices on the same substrate undergo identical fabrication conditions.

The measurement configuration is shown in Fig. 1(a). A low-frequency AC current, I_e, is driven from F_1 to the upper end of the Cu channel, and the nonlocal voltage V_{nl} is detected between F_2 and the lower end of the channel. The root-mean-square value of the AC current is consistently 0.3 mA in all nonlocal measurements. Figure 1(b) shows the nonlocal resistance $R_s = V_{nl}/I_e$ as a function of magnetic field B applied parallel to F_1 and F_2 stripes. The high and low states of R_s correspond to the parallel and antiparallel states of F_1 and F_2 magnetizations, respectively. The difference is the spin signal [22]

$$\Delta R_s = \frac{{P_e}^2 \rho_{\rm Cu} \lambda_{\rm Cu}}{A_{\rm Cu}} e^{-\frac{L}{\lambda_{\rm Cu}}}, \tag{1}$$

where P_e is the effective spin polarization of F_1 and F_2, $\rho_{\rm Cu}$ the Cu resistivity, $\lambda_{\rm Cu}$ the Cu spin-relaxation length, and $A_{\rm Cu}$ the Cu channel cross-sectional area. $\Delta R_s(T)$ of each NLSV is measured from 5 to 100 K, and Fig. 1(c) shows the data of device 11-43 (device 43 on chip 11). As T decreases, ΔR_s initially increases, reaching its maximum at 30 K, and then decreases. This feature is well documented [23–26] for NLSVs and convincingly attributed to the Kondo effect [12–15,27,28].

The resistivity $\rho_{\rm Cu}$ of a given NLSV is deduced from its Cu channel resistance $R_{\rm Cu}$, which is obtained by sending in an AC current of 0.1 mA through the channel and measuring the voltage difference between F_1 and F_2. The $\rho_{\rm Cu}(T)$ for device 11-43 is shown in Fig. 1(d), with $\rho_{\rm Cu} = 0.43\,\mu\Omega\,$cm at 5 K and $\rho_{\rm Cu} = 2.60\,\mu\Omega\,$cm at 295 K. The ratio of the two values (6.1) is the residual resistivity ratio (RRR). The inset of Fig. 1(d) shows the low-temperature portion of $\rho_{\rm Cu}(T)$. The low T increase of $\rho_{\rm Cu}$ indicates the Kondo effect from dilute magnetic impurities in Cu.

The coexistence of the resistivity upturn and the spin signal downtown at low temperatures unequivocally points to the Kondo effect. The former is a telltale sign of Kondo physics [2], and the magnitude of the upturn is proportional to the impurity concentration [28]. The latter was initially interpreted as being related to high surface spin-flip probabilities [23], but later works show strong evidence of the Kondo effect [12–14,27]. The Cu resistivity changes little below 30 K, and so should the surface scattering probability for electrons. Therefore the substantial decrease of spin signal below 30 K cannot be accounted for by a high surface spin-flip probability. In addition, as we show later in the text, both the $\rho_{\rm Cu}(T)$ and ${\tau_s}^{-1}(T)$ data can be fitted well by well-established Kondo physics formulas.

Previous work on NLSVs reported different spin signals measured on the opposite ends of the F_2 stripe [29]. However, such a difference is not present in our NLSV devices. The average $\lambda_{\rm Cu}$ ($>2\,\mu$m as shown in the next section) is significantly greater than the width (500 nm) of the Cu channel. Variations of spin accumulation across the channel width are negligible.

III. DATA ANALYSIS

Next we extract the average P_e and $\lambda_{\rm Cu}$ values of devices on the same substrate. ΔR_s versus L is plotted for ten devices on chip 11 at 30 K in Fig. 2(a). Fitting Eq. (1) to the plot yields $\lambda_{\rm Cu} = 2.6 \pm 0.1\,\mu$m and $P_e = 0.066 \pm 0.003$. The average $\rho_{\rm Cu}$ used in this process is deduced from the linear fitting to the $R_{\rm Cu}$ versus L data in Fig. 2(b). In this manner, the average P_e and $\lambda_{\rm Cu}$ are obtained between 5 and 100 K and shown in Fig. 2(c) and its inset, respectively. $\lambda_{\rm Cu}(T)$ resembles $\Delta R_s(T)$ in Fig. 1(c) and reaches its maximum of 2.6 μm at 30 K. $\lambda_{\rm Cu}$ decreases to 2.2 μm at 5 K because of the enhanced Kondo spin relaxation. The plot of $P_e(T)$ shows a rather flat trend at around 0.07 within the temperature range of our measurements. For NLSVs on chip 12, we obtain $\lambda_{\rm Cu} = 2.1 \pm 0.2\,\mu$m and $P_e = 0.064 \pm 0.006$ at 30 K. The trends of $\lambda_{\rm Cu}(T)$ and $P_e(T)$ are similar to those of chip 11.

As suggested by previous works on Py/Cu NLSVs, the Kondo effect originates from Fe impurities [12–14,27,28]. The maximum $\lambda_{\rm Cu}$ occurs at 30 K, which is the Kondo temperature T_K for Fe impurities in the Cu host. Data analysis of ${\tau_s}^{-1}(T)$ and ${\tau_e}^{-1}(T)$ later in the text is also consistent with $T_K = 30$ K. The Fe impurities are likely introduced in the fabrication processes. When the Py surface is ion milled, Fe atoms are removed and deposited on the sidewalls of the resist. When Cu is evaporated, the vapor flux of Cu transfers momentum to the Fe atoms on the sidewalls and redeposits them into the Cu channel. In some of the previous works [12,15,27,28], Fe impurities are concentrated near the Ohmic Py/Cu interfaces, and as a result, the spin polarization $P_e(T)$ is suppressed at low T. In our devices the Fe impurities are located throughout the Cu channel. This is evident from the low-T upturn of $\rho_{\rm Cu}(T)$, the low-T downturn of $\lambda_{\rm Cu}(T)$, and the flat trend of $P_e(T)$.

It is noticeable that data points disperse around the fitted lines in Figs. 2(a) and 2(b). For the two devices with $L = 3\,\mu$m, for example, data points of ΔR_s are above the fitted line and those of $R_{\rm Cu}$ are below. These indicate

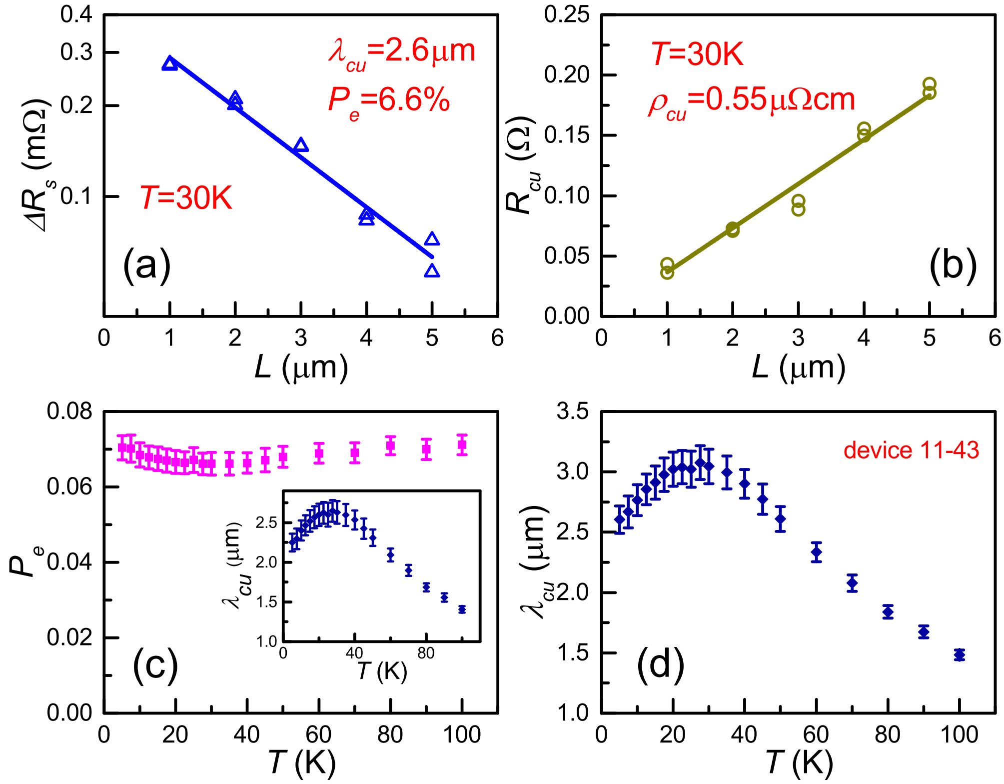

FIG. 2. (a) Spin signal ΔR_s and (b) Cu resistance R_{Cu} vs channel length L for NLSVs on chip 11 at 30 K. (c) Fitted average P_e and λ_{Cu} (inset) as a function of T. (d) λ_{Cu} vs T for device 11-43. The solid lines are fitting lines. The vertical axis of (a) is on a log scale.

variations of P_e, λ_{Cu}, and ρ_{Cu} between devices. Here we explore a method to extract the λ_{Cu} value from each NLSV. For a given NLSV on chip 11, the ρ_{Cu} is obtained directly from its Cu resistance. The fitted P_e values and uncertainties shown in Fig. 2(c) provide the range of P_e for devices on chip 11 at various temperatures. The λ_{Cu} of the NLSV at a specific T is then calculated from ΔR_s, P_e, and ρ_{Cu} by using Eq. (1), and the uncertainty of λ_{Cu} is properly propagated from the uncertainty of P_e and the measurement uncertainty of ΔR_s. $\lambda_{\mathrm{Cu}}(T)$ for device 11-43 is shown in Fig. 2(d) with a maximum $\lambda_{\mathrm{Cu}} = 3.0 \pm 0.1$ μm at 30 K. In this manner, $\lambda_{\mathrm{Cu}}(T)$ are obtained for all 20 NLSVs.

In Fig. 3, λ_{Cu} versus ρ_{Cu} at 30 K is plotted for all 20 NLSVs on chips 11 and 12. As ρ_{Cu} increases from 0.44 to 1.0 $\mu\Omega$ cm, λ_{Cu} clearly decreases from 3.0 to < 2.0 μm. This trend is qualitatively consistent with the Elliott-Yafet model. Since several spin-relaxation mechanisms with different spin-flip probabilities are involved, the decrease of λ_{Cu} is slower than a $1/\rho_{\mathrm{Cu}}$ dependence, which would be the case for a fixed spin-flip probability.

The spin-relaxation rate $\tau_s^{-1}(T)$ is calculated from $\lambda_{\mathrm{Cu}}(T)$ by using the relation $\lambda_{\mathrm{Cu}} = \sqrt{D\tau_s}$, shown in Figs. 4(a) and 4(b) for devices 11-33 and 12-32, respectively. $D = \frac{1}{3}v_F{}^2\tau_e$ is the diffusion constant, and $v_F = 1.57 \times 10^6$ m/s is the Fermi velocity of Cu. τ_e can be derived from ρ_{Cu} by using the Drude model $\rho_{\mathrm{Cu}} = m/(\tau_e n e^2)$, where $n = 8.47 \times 10^{28}$ m^{-3} is the Cu electron density, and m and e are electron mass and charge, respectively. With a decreasing T, $\tau_s{}^{-1}$ initially decreases, reaches its minimum at around 30 K, and then increases upon further cooling. This resembles the Kondo effect's low-temperature increase of ρ_{Cu}, as shown in the insets of Figs. 4(a) and 4(b). The low-T increase of ρ_{Cu} of 11-33 is much smaller than that of 12-32, indicating a lower impurity concentration in 11-33 [28]. However, the low-T increases of $\tau_s{}^{-1}$ of the two devices are surprisingly comparable. This provides the first hint of an unusual relation between Kondo momentum relaxation and Kondo spin relaxation.

To establish an overall trend, the low-T upturn of $\tau_s{}^{-1}$ is plotted versus that of ρ_{Cu} for all 20 NLSVs in Fig. 5. Strikingly, while $\Delta\rho_{\mathrm{Cu}}$ varies by more than an order of

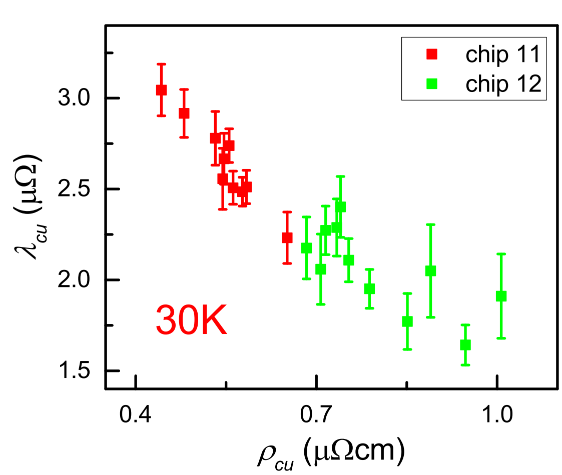

FIG. 3. The spin-relaxation length vs resistivity for NLSVs on chips 11 and 12.

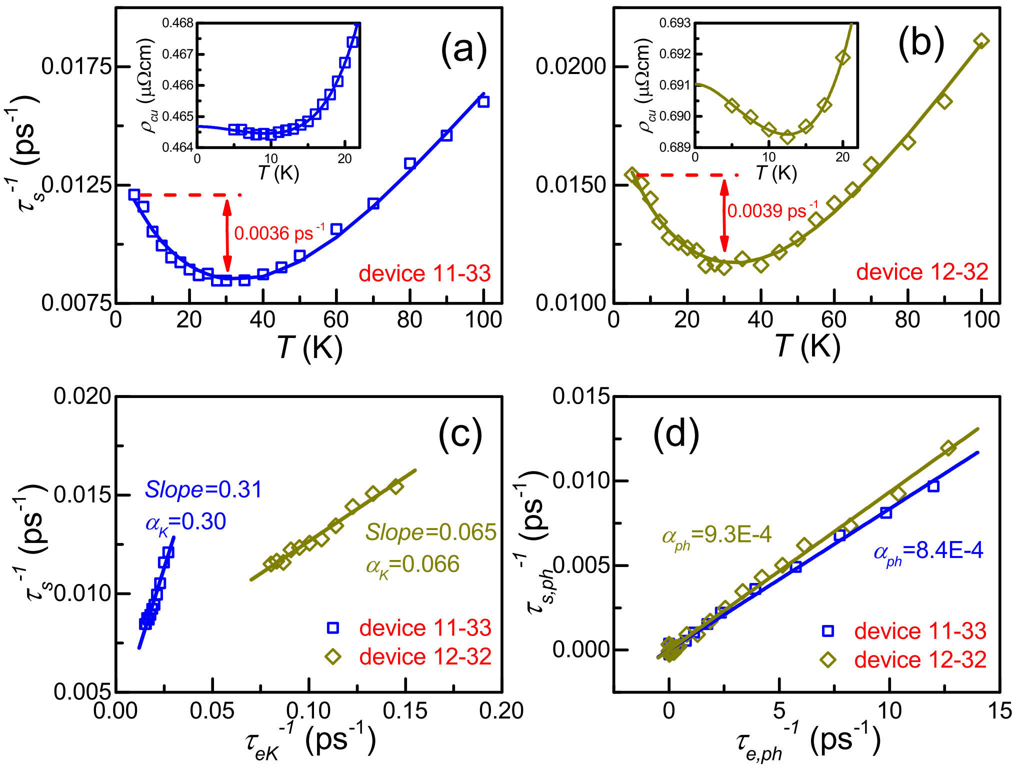

FIG. 4. Spin-relaxation rate τ_s^{-1} vs T for (a) device 11-33 and (b) device 12-32. $\rho_{\mathrm{Cu}}(T)$ plots are shown in the insets. (c) τ_s^{-1} vs τ_{eK}^{-1} for $T \leqslant 30$ K for the two devices. The slopes of the linear fittings are compared with α_K values obtained from fittings with Eq. (2). (d) $\tau_{s,ph}^{-1}$ vs $\tau_{e,ph}^{-1}$ plots. The solid lines are fitting lines.

magnitude between $1.2 \times 10^{-4}\,\mu\Omega\,\mathrm{cm}$ and $1.6 \times 10^{-3}\,\mu\Omega\,\mathrm{cm}$, $\Delta\tau_s^{-1}$ is confined between 0.003 and 0.0045 ps^{-1}, with no apparent dependence on $\Delta\rho_{\mathrm{Cu}}$. While $\Delta\rho_{\mathrm{Cu}}$ scales with the additional momentum-relaxation rate from the Kondo effect, $\Delta\tau_s^{-1}$ scales with the additional spin-relaxation rate from the Kondo effect. Note that $\Delta\rho_{\mathrm{Cu}}$ and $\Delta\tau_s^{-1}$ are extracted directly from $\rho_{\mathrm{Cu}}(T)$ and $\tau_s^{-1}(T)$ curves without any fitting. $\rho_{\mathrm{Cu}}(T)$ is measured by the lock-in method with long-time averaging, and the uncertainty is $<5 \times 10^{-5}\,\mu\Omega\,\mathrm{cm}$. The uncertainty of $\tau_s^{-1}(T)$ mainly comes from the uncertainty of $P_e(T)$. In the Supplemental Material (Note S1) [30], we show that the uncertainty of $P_e(T)$ moves the entire $\tau_s^{-1}(T)$ curve up or down but induces only small uncertainties in $\Delta\tau_s^{-1}$. While it is an intuitive assumption that τ_{sK}^{-1} is proportional to τ_{eK}^{-1}, Fig. 5 clearly demonstrates a different and unusual scaling.

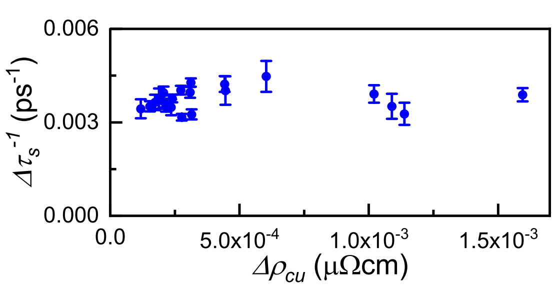

FIG. 5. The low-temperature increase of Cu spin-relaxation rate $\Delta\tau_s^{-1}$ vs the low-temperature increase of Cu resistivity $\Delta\rho_{\mathrm{Cu}}$.

In the following we show that the $\rho_{\mathrm{Cu}}(T)$ and $\tau_s^{-1}(T)$ data can be fitted by well-established models and the quantities of τ_{eK}^{-1} and τ_{sK}^{-1} can be extracted. Applying Matthiessen's rule to spin relaxation, the total τ_s^{-1} is given by $\tau_s^{-1} = \tau_{s,\mathrm{def}}^{-1} + \tau_{s,ph}^{-1} + \tau_{sK}^{-1}$, where $\tau_{s,\mathrm{def}}^{-1}$, $\tau_{s,ph}^{-1}$, and τ_{sK}^{-1} are the spin-relaxation rates attributed to defects, phonon, and Kondo effect, respectively. Defining $\tau_{e,\mathrm{def}}^{-1}$, $\tau_{e,ph}^{-1}$, and τ_{eK}^{-1} as the corresponding momentum-relaxation rates and α_{def}, α_{ph}, and α_K as the associated spin-flip probabilities, we have

$$\frac{1}{\tau_s(T)} = \alpha_{\mathrm{def}}\frac{1}{\tau_{e,\mathrm{def}}} + \alpha_{ph}\frac{1}{\tau_{e,ph}(T)} + \alpha_K\frac{1}{\tau_{eK}(T)}. \tag{2}$$

It is well justified to assume a linear relation between τ_s^{-1} and τ_e^{-1} for defects and phonons, because the EY mechanism is dominant. We will show later that τ_{sK}^{-1} is also proportional to τ_{eK}^{-1} under varying T.

The τ_e^{-1} of each type (total, defect, phonon, or Kondo) is linked to the corresponding ρ by the Drude model. The defect resistivity ρ_{def} is T independent, and the phonon resistivity can be described as $\rho_{ph}(T) = AT^5$ at low T, where A is a constant related to the Debye temperature [31]. The Kondo resistivity can be described by a phenomenological formula [9]

$$\rho_K(T) = \rho_{K0}\left(\frac{T_K'^2}{T^2 + T_K'^2}\right)^s, \tag{3}$$

where $T_K' = T_K/\sqrt{2^{1/s}-1}$, $s = 0.225$, and $T_K = 30$ K. From ${\tau_e}^{-1} = {\tau_{e,\mathrm{def}}}^{-1} + {\tau_{e,ph}}^{-1} + {\tau_{sK}}^{-1}$, the total resistivity is

$$\rho_{\mathrm{Cu}}(T) = \rho_{\mathrm{def}} + AT^5 + \rho_K(T). \tag{4}$$

Fitting Eq. (4) along with Eq. (3) to the measured $\rho_{\mathrm{Cu}}(T)$ data below 20 K yields ρ_{def}, A, and ρ_{K0}. The fitting does not work well for $T > 20$ K, because $\rho_{ph}(T) = AT^5$ is only valid at low T. For the data of 11-33 and 12-32 in the insets of Figs. 4(a) and 4(b), the fitted values of ρ_{K0} are 0.0013 and 0.0067 $\mu\Omega$ cm, respectively. ρ_{K0} or ${\tau_{eK0}}^{-1}$ represents the ρ_K or ${\tau_{eK}}^{-1}$ value at $T << T_K$.

Despite the small magnitudes of ρ_{K0}, the fitted values are of high confidence. The curves are fitted well by Eq. (4). The three terms have distinct temperature dependence and can be clearly resolved. With an increasing T, ρ_{def} remains a constant, $\rho_K(T)$ decreases, and $\rho_{ph}(T) = AT^5$ increases. The fitted ρ_{def} ranges between 0.4 and 1.0 $\mu\Omega$ cm among 20 devices. Such variations, which are temperature independent, have no impact on the low-T upturn and fitted ρ_{K0}. The fitted ρ_{K0} varies by a factor of 10 between 0.001 and 0.01 $\mu\Omega$ cm and shows no apparent dependence on ρ_{def}.

To extract α_{def}, α_{ph}, and α_K, we fit Eq. (2) to the ${\tau_s}^{-1}(T)$ data by using the empirical data of ${\tau_{e,\mathrm{def}}}^{-1}$, ${\tau_{e,ph}}^{-1}(T)$, and ${\tau_{eK}}^{-1}(T)$ obtained from the measured $\rho_{\mathrm{Cu}}(T)$ and fitting. More specifically, ${\tau_{e,\mathrm{def}}}^{-1}$ can be obtained from the fitted ρ_{def} and ${\tau_{eK}}^{-1}(T)$ from the fitted ρ_{K0} and Eq. (3). For ${\tau_{e,ph}}^{-1}(T)$ we use the relation $\rho_{ph}(T) = \rho_{\mathrm{Cu}}(T) - \rho_{\mathrm{def}} - \rho_K(T)$. We do not use $\rho_{ph}(T) = AT^5$, because it significantly deviates from the experimental data when $T > 20$ K. The empirical data sets of ${\tau_{e,\mathrm{def}}}^{-1}$, ${\tau_{e,ph}}^{-1}(T)$, and ${\tau_{eK}}^{-1}(T)$ are substituted into Eq. (2). The fitting procedure automatically adjusts the parameters α_{def}, α_{ph}, and α_K until the generated ${\tau_s}^{-1}(T)$ curve provides the best fit to the experimental ${\tau_s}^{-1}(T)$ data. The best fits for α_K are 0.30 ± 0.03 and 0.066 ± 0.006, and the best fits for α_{ph} are $(8.4 \pm 0.3) \times 10^{-4}$ and $(9.3 \pm 0.4) \times 10^{-4}$ for devices 11-33 and 12-32, respectively. While the α_{ph} values are comparable, the α_K values are quite different. Again, the results point to the unusual scaling for Kondo spin relaxation.

We should justify the assumed linear relation ${\tau_{sK}}^{-1}(T) = \alpha_K {\tau_{eK}}^{-1}(T)$ under varying T in Eq. (2). In Fig. 4(c), ${\tau_s}^{-1}$ is plotted versus ${\tau_{eK}}^{-1}$ between 5 and 30 K for the two NLSVs, and we observe clear linear dependences. At $T \leqslant 30$ K, the variation of ${\tau_s}^{-1}$ should be dominated by ${\tau_{sK}}^{-1}$, because ${\tau_{s,\mathrm{def}}}^{-1}$ is T independent and ${\tau_{s,ph}}^{-1}$ is negligible compared to ${\tau_{sK}}^{-1}$. Therefore Fig. 4(c) confirms the linear relation between ${\tau_{sK}}^{-1}(T)$ and ${\tau_{eK}}^{-1}(T)$ under varying T. In addition, the slopes of the linear fittings to the ${\tau_s}^{-1}$ versus ${\tau_{eK}}^{-1}$ data are very close to the fitted α_K values using Eq. (2). Similarly, the linear relation for phonons between ${\tau_{s,ph}}^{-1}(T)$ and ${\tau_{e,ph}}^{-1}(T)$ is also verified in Fig. 4(d). The data of ${\tau_{s,ph}}^{-1}$ is obtained by subtracting $\alpha_{\mathrm{def}} {\tau_{e,\mathrm{def}}}^{-1}$ and $\alpha_K {\tau_{eK}}^{-1}$ from the total ${\tau_s}^{-1}$. The slopes of the fitted lines are the same as the fitted α_{ph} values by using Eq. (2).

Next we demonstrate the unusual relation between ${\tau_{sK}}^{-1}$ and ${\tau_{eK}}^{-1}$ under a varying impurity concentration C_{Fe} which is proportional to ρ_{K0} or ${\tau_{eK0}}^{-1}$ [28]. Figure 6 shows the fitted α_K versus ρ_{K0} for all 20 NLSVs. Strikingly, α_K decreases drastically from 0.44 ± 0.05 to 0.045 ± 0.004 as ρ_{K0} ($\propto {\tau_{eK0}}^{-1}$) increases from <0.001 $\mu\Omega$ cm to >0.009 $\mu\Omega$ cm.

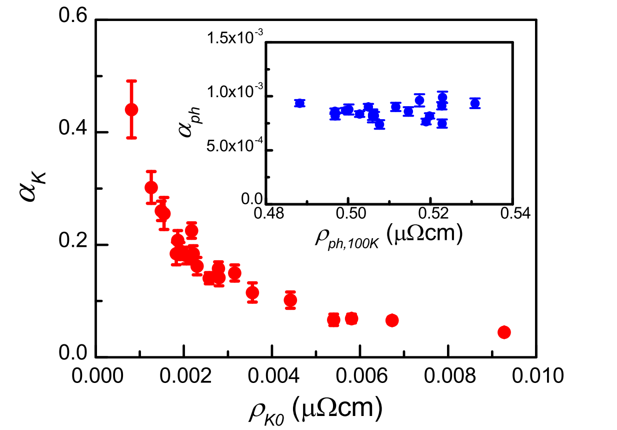

FIG. 6. Kondo spin-flip probability α_K vs Kondo resistivity ρ_{K0}. Inset: Phonon spin-flip probability α_{ph} vs 100-K phonon resistivity $\rho_{ph,100\mathrm{K}}$.

As a comparison, the inset of Fig. 6 shows α_{ph} versus $\rho_{ph,100\mathrm{K}}$, which is the ρ_{ph} at 100 K, for all NLSVs. α_{ph} remains nearly a constant and independent of $\rho_{ph,100\mathrm{K}}$, as expected for processes governed by the EY mechanism. The average α_{ph} ($\sim 8.5 \times 10^{-4}$) is in good agreement with previous works [15,26,32]. The average α_{def} is 3.2×10^{-4}, and the data are shown in the Supplemental Material (Note S2) [30].

The decreasing trend in Fig. 6 suggests that the relation between ${\tau_{sK0}}^{-1}$ and ${\tau_{eK0}}^{-1}$ is not linear, where ${\tau_{sK0}}^{-1}$ is the value of ${\tau_{sK}}^{-1}$ at $T \ll T_K$. Figure 7(a) shows ${\tau_{sK0}}^{-1}$, obtained by using the definition ${\tau_{sK0}}^{-1} = \alpha_K {\tau_{eK0}}^{-1}$, versus ${\tau_{eK0}}^{-1}$. While ${\tau_{eK0}}^{-1}$ varies by a factor of 10, ${\tau_{sK0}}^{-1}$ stays nearly constant, clearly defying a linear dependence. This relation obtained from the fitting method is quite consistent with the $\Delta{\tau_s}^{-1}$ versus $\Delta\rho_{\mathrm{Cu}}$ dependence, which is extracted directly

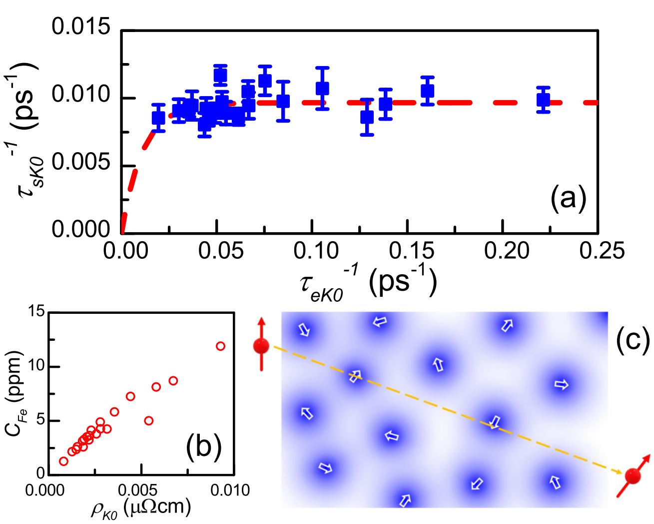

FIG. 7. (a) Kondo spin-relaxation rate ${\tau_{sK0}}^{-1}$ vs Kondo momentum-relaxation rate ${\tau_{eK0}}^{-1}$ from 20 NLSVs. (b) Fe impurity concentration C_{Fe} vs ρ_{K0}. (c) Illustration of the Kondo medium. The gray scale indicates the spin density, and the white arrows indicate the polarization directions of the domains.

from the experimental $\rho_{\mathrm{Cu}}(T)$ and $\tau_s^{-1}(T)$ curves and shown in Fig. 5.

The few previous theoretical treatments of Kondo spin relaxation assume a linear relation and yield a constant α_K of 2/3 [2,28]. The high spin-flip probability is a reflection of the antiferromagnetic nature of the exchange process. The relations shown in Figs. 6 and 7(a) deviate from this prediction and have been neither anticipated nor addressed previously. These plots with horizontal error bars are available in the Supplemental Material (Note S3) [30]. Based on previous theoretical works, Kim *et al.* showed explicitly that the expression of ρ_{K0} or $\tau_{eK0}{}^{-1}$ is proportional to the impurity concentration C_{Fe} [28]. The C_{Fe} for each NLSV can be extracted from the temperature T_{min} that corresponds to the minimum of the fitted $\rho_{\mathrm{Cu}}(T)$ curve [27,33]. The range of C_{Fe} in our devices is between 1 and 12 ppm, which is significantly lower than the 100–200 ppm by Hamaya *et al.* [14]. Figure 7(b) shows the extracted C_{Fe} versus ρ_{K0} for all NLSVs. Therefore Fig. 7(a) suggests that Kondo spin relaxation remains nearly constant as the impurity concentration increases by one order of magnitude. The interactions between impurity spins should be negligible because C_{Fe} is very dilute and <12 ppm, as shown in Fig. 7(b).

IV. PHYSICAL PICTURES

The unusual scaling can be understood by considering the Kondo clouds, which act as momentum-scattering barriers as well as spin-scattering barriers for conduction electrons passing through them [34]. While $\tau_{eK}{}^{-1}$ should be proportional to the average charge density, $\tau_{sK}{}^{-1}$ should be proportional to the average spin density of the cloud. $\tau_{sK}{}^{-1}$ may also be related to the relative orientation between the conduction electron spin and the polarization direction of the cloud.

The size of a single Kondo cloud is $\xi_K = \sqrt{\hbar D/k_B T_K} \approx$ 100 nm for diffusive Cu channels. The average distance between Fe impurities is 10 nm $< d_{\mathrm{Fe}} <$ 20 nm, estimated from the C_{Fe} of our NLSVs, and obviously $\xi_K > d_{\mathrm{Fe}}$. Therefore the Kondo clouds from adjacent impurities overlap and form a continuous medium in the Cu channel. The charge density of overlapping clouds should simply add up. However, the spin density may cancel out, because the polarization directions of the clouds are random. Figure 7(c) is a cartoon illustration of the spatial distributions of spin density and polarization directions of the Kondo medium. Domains with random polarization directions are formed in the medium around impurity sites.

When a conduction electron traverses through the medium, $\tau_{eK0}{}^{-1}$ or $\tau_{sK0}{}^{-1}$ should be proportional to the average charge density or the average spin density of the medium, respectively, along the electron's path. The influence of the polarization directions on $\tau_{sK0}{}^{-1}$ can be neglected, because the traversing electron passes through many ($\approx 10^4$) randomly oriented Kondo domains within the time of τ_{sK0}. A higher C_{Fe} leads to a higher charge density and a higher $\tau_{eK0}{}^{-1}$, but not necessarily to a higher spin density or $\tau_{sK0}{}^{-1}$ because of the cancellation effect of overlapping clouds. The exact trend is challenging to predict without precise knowledge of the spatial distributions of spin and charge densities of the Kondo medium. From Fig. 7(a), we infer that the average spin density of the medium maintains a nearly constant value within the range of 1 ppm $< C_{\mathrm{Fe}} <$ 12 ppm, corresponding to 10 nm $< d_{\mathrm{Fe}} <$ 20 nm. The red curve in Fig. 7(a) is a guide to the eye with the assumption that $\tau_{sK0}{}^{-1} \to 0$ as $\tau_{eK0}{}^{-1} \to 0$. We speculate that the initial slope of the curve, representing α_K in the limit of $\tau_{eK0}{}^{-1} \to 0$, should be the theoretically predicted 2/3 [2,28].

V. CONCLUSIONS

In conclusion, we extract the Kondo momentum-relaxation rate $\tau_{eK0}{}^{-1}$ and the Kondo spin-relaxation rate $\tau_{sK0}{}^{-1}$ from Cu-based nonlocal spin valves with Fe impurities. While $\tau_{eK0}{}^{-1}$ is tuned by a factor of ten by varying Fe concentrations, $\tau_{sK0}{}^{-1}$ remains nearly constant and defies a more intuitive linear dependence on $\tau_{eK0}{}^{-1}$. Such a relation can be understood by considering spin relaxation through overlapping Kondo clouds and provides evidence for the Kondo screening clouds.

[1] W. J. De Haas and G. J. Van Den Berg, Physica **3**, 440 (1936).
[2] J. Kondo, Prog. Theor. Phys. **32**, 37 (1964).
[3] V. Chandrasekhar, C. Van Haesendonck, and A. Zawadowski, *Kondo Effect and Dephasing in Low-Dimensional Metallic Systems* (Kluwer Academic Publishers, Dordrecht, the Netherlands, 2000).
[4] I. Affleck, arXiv:0911.2209.
[5] E. S. Sorensen and I. Affleck, Phys. Rev. B **53**, 9153 (1996).
[6] J. B. Boyce and C. P. Slichter, Phys. Rev. Lett. **32**, 61 (1974).
[7] M. A. Blachly and N. Giordano, Phys. Rev. B **51**, 12537 (1995).
[8] I. V. Borzenets, J. Shim, J. C. H. Chen, A. Ludwig, A. D. Wieck, S. Tarucha, H. S. Sim, and M. Yamamoto, Nature (London) **579**, 210 (2020).
[9] D. Goldhaber-Gordon, J. Gores, M. A. Kastner, H. Shtrikman, D. Mahalu, and U. Meirav, Phys. Rev. Lett. **81**, 5225 (1998).
[10] M. Johnson and R. H. Silsbee, Phys. Rev. Lett. **55**, 1790 (1985).
[11] F. J. Jedema, A. T. Filip, and B. J. van Wees, Nature (London) **410**, 345 (2001).
[12] L. O'Brien, M. J. Erickson, D. Spivak, H. Ambaye, R. J. Goyette, V. Lauter, P. A. Crowell, and C. Leighton, Nat. Commun. **5**, 3927 (2014).
[13] J. T. Batley, M. C. Rosamond, M. Ali, E. H. Linfield, G. Burnell, and B. J. Hickey, Phys. Rev. B **92**, 220420(R) (2015).
[14] K. Hamaya, T. Kurokawa, S. Oki, S. Yamada, T. Kanashima, and T. Taniyama, Phys. Rev. B **94**, 140401(R) (2016).
[15] J. D. Watts, L. O'Brien, J. S. Jeong, K. A. Mkhoyan, P. A. Crowell, and C. Leighton, Phys. Rev. Materials **3**, 124409 (2019).
[16] R. J. Elliott, Phys. Rev. **96**, 266 (1954).
[17] Y. Yafet, Phys. Lett. A **98**, 287 (1983).
[18] M. I. Dyakonov and V. I. Perel, Sov. Phys. Solid State USSR **13**, 3023 (1972).

[19] X. J. Wang, H. Zou, L. Ocola, and Y. Ji, Appl. Phys. Lett. **95**, 022519 (2009).
[20] Y. J. Cai, Y. M. Luo, C. Zhou, C. Qin, S. H. Chen, Y. Z. Wu, and Y. Ji, J. Phys. D **49**, 185003 (2016).
[21] G. L. Chen and N. Giordano, Phys. Rev. Lett. **66**, 209 (1991).
[22] M. Johnson, Phys. Rev. Lett. **70**, 2142 (1993).
[23] T. Kimura, T. Sato, and Y. Otani, Phys. Rev. Lett. **100**, 066602 (2008).
[24] G. Mihajlovic, J. E. Pearson, S. D. Bader, and A. Hoffmann, Phys. Rev. Lett. **104**, 237202 (2010).
[25] H. Zou and Y. Ji, Appl. Phys. Lett. **101**, 082401 (2012).
[26] E. Villamor, M. Isasa, L. E. Hueso, and F. Casanova, Phys. Rev. B **87**, 094417 (2013).
[27] L. O'Brien, D. Spivak, J. S. Jeong, K. A. Mkhoyan, P. A. Crowell, and C. Leighton, Phys. Rev. B **93**, 014413 (2016).
[28] K. W. Kim, L. O'Brien, P. A. Crowell, C. Leighton, and M. D. Stiles, Phys. Rev. B **95**, 104404 (2017).
[29] T. Kimura and Y. Otani, J. Phys.: Condens. Matter **19**, 165216 (2007).
[30] See Supplemental Material at http://link.aps.org/supplemental/10.1103/PhysRevB.104.085101 for error analysis and additional data.
[31] J. M. Ziman, *Electrons and Phonons* (Clarendon Press, Oxford, 1960).
[32] P. Monod and F. Beuneu, Phys. Rev. B **19**, 911 (1979).
[33] J. P. Franck, D. L. Martin, and F. D. Manchester, Proc. R. Soc. London, Ser. A **263**, 494 (1961).
[34] P. Simon and I. Affleck, Phys. Rev. B **68**, 115304 (2003).